Geometrically Stabilized Skyrmionic Vortex in FeGe Tetrahedral Nanoparticles

Kodai Niitsu (koudai.niitsu@riken.jp)
RIKEN https://orcid.org/0000-0002-0430-8868

Yizhou Liu
RIKEN

Alexander Booth
University of New Hampshire

Xiuzhen Yu
RIKEN https://orcid.org/0000-0003-3136-7289

Nitish Mathur
University of Wisconsin-Madison

Matthew Stolt
University of Wisconsin-Madison

Daisuke Shindo
RIKEN

Song Jin
University of Wisconsin-Madison https://orcid.org/0000-0001-8693-7010

Jiadong Zang
University of New Hampshire

Naoto Nagaosa
The University of Tokyo/RIKEN

Yoshinori Tokura
RIKEN https://orcid.org/0000-0002-2732-4983

Article

Keywords: magnetism, topology, skyrmion

Posted Date: March 17th, 2021

DOI: https://doi.org/10.21203/rs.3.rs-311043/v1

Version of Record: A version of this preprint was published at Nature Materials on January 27th, 2022. See the published version at https://doi.org/10.1038/s41563-021-01186-x.

Geometrically Stabilized Skyrmionic Vortex in FeGe Tetrahedral Nanoparticles

Authors: K. Niitsu[1,2*,†], Y. Liu[1†], A. C. Booth[3], X. Z. Yu[1], N. Mathur[4], M. J. Stolt[4], D. Shindo[1], S. Jin[4], J. Zang[3*], N. Nagaosa[1,5], Y. Tokura[1,5,6]

Affiliations:

[1]RIKEN Center for Emergent Matter Science (CEMS), Wako, Japan.

[2]Department of Materials Science and Engineering, Kyoto University, Sakyo-ku, Japan.

[3]Department of Physics and Astronomy, University of New Hampshire, Durham, NH, USA.

[4]Department of Chemistry, University of Wisconsin-Madison, Madison, WI, USA.

[5]Department of Applied Physics, University of Tokyo, Bunkyo-ku, Japan.

[6]Tokyo College, University of Tokyo, Bunkyo-ku, Japan.

†Equal contribution

*Correspondence to: niitsu.koudai.8z@kyoto-u.ac.jp and Jiadong.Zang@unh.edu

Abstract: The concept of topology has dramatically expanded the landscape of magnetism, leading to the discovery of numerous magnetic textures with intriguing topological properties. A magnetic skyrmion is an emergent topological magnetic texture with a string-like structure in three dimensions and a disk-like structure in one and two dimensions. Skyrmions in zero dimensions have remained elusive owing to challenges from many competing orders. Herein, by integrating electron holography and micromagnetic simulations, we uncover the real-space magnetic configurations of a novel skyrmionic vortex structure confined in a B20-type FeGe tetrahedral nanoparticle. This texture shows excellent robustness against temperature without applying a magnetic field; an isolated skyrmionic vortex forms at the ground state. These findings shed light on zero-dimensional geometrical confinement as a route to engineer and manipulate individual skyrmionic metastructures.

Magnetic structures in confined geometries have been a versatile platform for realizing their vast potential in diverse applications. In particular, engineering of magnetic structures has been intensively studied in two- and one-dimensionally shaped ferromagnets, wherein the magnetic domain structures accommodate their own physical and microstructural features into reduced dimensions[1,2]. In contrast, although confined in zero dimensions, i.e., in nanoparticles, sophisticated three-dimensional (3D) magnetic structures can still develop under appropriate conditions, which have not been as well studied because of technical difficulties in visualizing 3D magnetic configurations inside a single nanoparticle.

Meanwhile, the Dzyaloshinskii–Moriya interaction has provided a vast playground to tailor topological states in magnetic systems. One of the most remarkable advances has been the discovery of magnetic skyrmions, which are topological swirling spin configurations that are typically stabilized in material systems with broken inversion symmetry[3-5]. Their topological-particle like nature in two dimensions and the extremely low critical current density needed to drive their motion have potential for manipulating individual skyrmions in future spintronic devices[6-12]. To enable their practical applications, methods to isolate a skyrmion from the skyrmion lattice or other competing magnetic states have been intensively explored[13-17]. One of the most promising methods for skyrmion isolation is geometrical confinement in low dimensions[8-22]. Skyrmions prefer thinner and narrower hosts with limited out-of-plane magnetic fields and thermal excitations[20]. In this sense, nanoparticles with strong geometrical confinement are expected to be a promising host for isolated skyrmions. However, in nanoparticles with specific symmetries, the interplay of the bulk chiral spin interactions and geometrical symmetry invokes chiral geometrical frustration, especially when the geometrical size of the nanoparticle is comparable to the helimagnetic wavelength. This new class of frustration may provide an additional degree of freedom to realize novel magnetic structures. Therefore, the visualization of emergent magnetic configurations in a single nanoparticle could provide novel insight into the role of geometrical confinement as well as a technical advancement in real-space magnetic imaging.

In this study, we developed and performed multi-angle electron holography (EH) on chemically-synthesized isolated tetrahedral nanoparticles of B20-type FeGe to reveal

the internal 3D magnetic configurations. Integrating EH observations and micromagnetic simulations uncovered the real-space magnetic configurations that dramatically change with particle size. Although larger nanoparticles reasonably host the helimagnetic ground state, nanoparticles with sizes comparable to the helical wavelength [~70 nm for FeGe[20]] lead to the emergence of a novel skyrmionic vortex structure, revealing the topological nature of a skyrmion string. This texture shows excellent robustness against temperature without applying a magnetic field; the zero-field skyrmionic ground state is realized for a certain size range of nanoparticles.

Morphology and crystallography of the synthesized nanoparticles

Scanning electron microscopy (SEM) images and an X-ray diffraction (XRD) pattern of the products synthesized using a chemical vapor deposition (CVD) method are presented in Fig. 1a,b. The products were composed of various morphologies such as tetrahedra, octahedra, and rounded/faceted nanowires. Most were indexed as the B20 cubic crystal structure of FeGe, except for one peak in the XRD pattern assigned to the hexagonal FeGe crystal structure of the well-faceted nanowires[19]. The crystallography and crystallinity of the highly symmetric tetrahedral nanoparticles with various sizes from approximately 100 nm to over 500 nm (Fig. 1a, right column) were identified using the conventional transmission electron microscopy (TEM) observations, the multi-angle EH observations, and the nanobeam diffraction technique (Fig. 1c–n). According to the conventional TEM observations (Fig. 1f–h), which were obtained from the three representative projections in Fig. 1c–e, the particle consisted of a well-crystalline body with a high tetrahedral symmetry and less-crystalline (most likely amorphous) surfaces with a thickness of ~10 nm. In the corresponding phase images (Fig. 1i–k), as the phase undulations in the paramagnetic state were qualitatively identical to the thickness variations, the different phase variations (Fig. 1j,k) enable the two projections (Fig. 1g,h) to be distinguished. A systematic set of diffraction patterns of the nanoparicles (Fig. 1l–n) was unambiguously assigned to the B20 cubic structure with the tetrahedral facets in the $\{111\}$ planes. The crystallography was consistent with the XRD pattern for the synthesized products (Fig. 1b).

Multi-angle EH observation of skyrmionic vortex

EH studies for visualizing magnetic textures were performed for the [010], [01$\bar{1}$], and [00$\bar{1}$] projections. The most striking magnetization texture appears in a tetrahedral nanoparticle with a size of 145 nm (Fig. 2a) at 10 K, whose corresponding TEM images are presented in Fig. 2c–e. Systematic EH imaging reveals a swirling in-plane magnetic flux along the [00$\bar{1}$] direction (Fig. 2f), a distorted swirling in-plane magnetic flux along the [01$\bar{1}$] direction (Fig. 2g), and an unconventional magnetic flux distribution along the [010] direction (Fig. 2h). Figure 2i–k are the corresponding projections for the magnetic phase distribution calculated from micromagnetic simulations in a tetrahedral nanoparticle of the same size (see Methods and Supplementary Note 2 for details). The simulation well captures the essential features of the observed magnetic texture. The difference between the phase shift profiles along the lines in Figs. 2f and 2i is within reason (Fig. 2b). The phase shift in the simulation is underestimated because it does not account for the possible contribution from the amorphous surface layer.

The simulated 3D magnetic configuration, we herein named the skyrmionic vortex, is detailed in Fig. 2l–n and the Supplementary Movies. Its non-triviality is indicated by both the tube-like equi-spin surface and the projected magnetic configuration. The equi-spin surface with the *z*-component (along [001] direction) of magnetization S_z = 0 forms a tube stretching along the [001] direction (Fig. 2m). The in-plane magnetic configurations also show that the tube in the skyrmionic vortex state forms in each cross section (Fig. 2m,n). The projected magnetic configuration along the [00$\bar{1}$] direction (Fig. 2l) resembles a vortex state with unity vorticity, in which in-plane magnetic moments rotate by an angle of 2π circulating around the center. A unity vorticity state can be either a singularity, meron or skyrmion[23]. The magnetic moments here are well defined everywhere; therefore, it cannot be a singularity. Furthermore, unlike meron states, the magnetic moments herein flip their *z*-components from the center to the periphery. The emergence of skyrmionic texture in this tetrahedron is further evidenced by the topological charge calculation, as detailed in the Supplementary Note 1. In general, confined geometries have finite boundaries, and topological charge is no longer strictly integer-valued. By excluding the corner spin twists, the total topological charge enclosed

by the dashed box in Fig. 2l has a fractional value of 0.93. Its slight deviation from 1 is mainly attributed to the entanglement with corner spin twists at the boundary of the skyrmionic vortex.

The skyrmionic vortex tube exhibits a richer structure than conventional skyrmion tubes. Although the core spins of skyrmionic vortex passes through the [001] direction uniformly, the peripheral swirling pitch does not. A Bloch-like rotation with a wider pitch is present in the central cross section, a Néel-like rotation with a narrower pitch is emergent near the top and bottom, and mixed helicities are formed in between, altogether giving rise to the appearance of a potbelly-shaped equi-spin surface. In addition, a topological defect known as a fractional vortex[24] also forms on the edge owing to chiral geometric frustration, i.e., the interplay between the geometrical confinement of the tetrahedron and the bulk helimagnetic interaction (greater details on the chiral geometric frustration will be given in the next section). The two fractional vortices on the top and bottom edges are connected through a vertical line with spins pointing in the [001] direction (Fig. 2n) and facilitate the formation of the skyrmionic vortex tube.

With this portrait of the skyrmionic vortex, we can now readily interpret the observed and simulated projections (Fig. 2f–k) as follows: the $[00\bar{1}]$ projections (Fig. 2f,i) are identical to the top view of this skyrmionic vortex, capturing the swirling contrasts. The [010] projections (Figs. 2h and 2k) are the side view, with the [001] polarity of the core color-coded with the yellow bars. The $[01\bar{1}]$ projections (Fig. 2g,j) are the intermediate projections, mixing the features of the top and side views and thus showing a distorted swirling texture. A detailed 3D view of the skyrmionic vortex can also be found in the Supplementary Movies.

A variation of the observed and simulated in-plane magnetic flux projections for nanoparticles with various sizes is presented in Fig. 3. The series of EH observations of a nanoparticle further reduced in size (110 nm, Fig. 3a) still captures similar characteristics to those of the 145-nm nanoparticle except for the [010] projection. The simulated results for this size again reveal the skyrmionic vortex with the in-plane winding and $[00\bar{1}]$ polarization reversal, as shown in the cross-sectional view. The projections reproduce some essential features of the observation although being deficient in capturing the delicate features. Excellent agreement between the observations and

simulations is demonstrated for the nanoparticle with a size of 185 nm (Fig. 3b). The magnetic configuration therein comprises three skyrmionic vortices, with the longest one formed along the [001] direction and the other two terminating at a side edge, as shown in the cross-sectional view. The core magnetization of all three vortices points in the same [001] direction, whereas the spacing between vortices has magnetization mostly in the $[00\bar{1}]$ direction. The important discrete nature of these skyrmionic states further supports their topological nature. Even larger nanoparticles host the helimagnetic state, which is the ground state in bulk[20]. As the particle size increases (Fig. 3c,d), there is also a transition of the helical wavevector (q) from along the <100> to <111> direction. This transition is primarily driven by the competition between magneto-crystalline anisotropy and dipole–dipole interactions. Details of the energy analysis are given in the Supplementary Note 2.

Edge spin twists, fractional vortices, and skyrmion tube: Role of chiral geometric frustration

The formation of a skyrmionic vortex is closely related to the edge spin twists and topological defects formed at the edge of a tetrahedron. These defect states are induced by the chiral geometric frustration originating from the interplay between the tetrahedral geometry and the chiral spin interactions. It is a generic scheme that at surfaces and edges of any geometry, the symmetry of bulk spin interactions is broken because of missing neighbouring lattice sites and/or the presence of defects and irregular lattice sites[25,26]. Taking the helimagnet plane shown in Fig. 4a as an example, the zero-field ground state is a helical state and parallel helical stripes (black arrows) are developed. Enabled by the DM interaction, the missing neighbours at the boundaries perpendicular to the helical stripes (here the left and right boundaries) gives rise to edge spin twists (indicated by the red arrows), in which spins point along the edge and close the magnetic flux of the adjacent helical strip. Such edge spin twists have already been observed experimentally in FeGe nanostripes[14,15]. Once the plane is folded and a new edge is created (Fig. 4b), the helical stripes are broken into two parts, and geometrical frustration occurs; the left plane favours the edge twist indicated by the left dashed arrows, whereas the right plane does the edge twist indicated by the right dashed arrows. Such geometric frustration of chiral

origin, or '*chiral geometric frustration*', gives rise to a new type of edge spin twist as shown in Fig. 4b (solid blue arrows and dot). Intrinsic chiral geometric frustration is a natural consequence for any edge in chiral magnets.

To be more specific for a tetrahedral nanoparticle, in the [100] helix, spin stripes on the (111) facet of the tetrahedron end up on the top edge, as illustrated in Fig. 4c. Similar to the 1D nanostripe case, an edge spin twist is thus expected to form on the edge. However, the [100] helix also forms spin stripes on the neighbouring $(11\bar{1})$ facet. A similar edge spin twist with opposite direction is expected. Two counter-propagating spin twists on the same edge lead to the chiral geometric frustration and give rise to the Néel-like edge spin twists at the red edge (Fig. 4d). In this sense, the physics here does inherit the edge twist physics in 1D nanostripes but with another spatial degree of freedom because of the 3D nature of the tetrahedron (although this system is confined in zero dimension).

The formation of the skyrmionic vortex is closely related to the edge spin twists in small tetrahedra. Each edge of the tetrahedron adjoins two lateral surfaces, thus suffering from the chiral geometric frustration as well. As shown in Fig. 4e, the top edge (red line) adjoins (111) and $(11\bar{1})$ facets of the tetrahedron. To compensate spin twists from adjacent surfaces, half spins on the edge take one direction, and the other half take the opposite (Fig. 4e). Two counter-propagating spin twists meet at the midpoint of the edge, and a Néel-type domain wall emerges. In the $(1\bar{1}0)$ plane containing the bottom edge and midpoint of the top edge (Fig. 4f), the Néel-type domain wall together with spins along the $[00\bar{1}]$ direction resembles a fractional vortex on the bottom edge; the (110) plane (Fig. 4g) also hosts a fractional vortex on the top edge. Each fractional vortex carries a winding number of $-1/2$ in the plane. In contrast to the findings in previous studies [e.g., ref. [24]], the fractional vortices formed here are mainly stabilized by the DM interaction rather than the magnetic dipole–dipole interaction. Two fractional vortices are connected via a vertical line on which spins point in the $[00\bar{1}]$ direction. This line comprises the spine of the skyrmionic tube. That is the reason why the skyrmionic tube ends at two opposite edges. Hence, the formation of skyrmionic vortices can be mainly attributed to the chiral geometric frustration.

Indeed, we can capture the essential feature of the Néel-like edge spin twists

forming various types of magnetic and topological orders. Lower panels of Fig. 4h–j represent the simulated 3D spin configurations for 145-, 255-, and 300-nm tetrahedra forming 2, 4, and 3 twisted edges highlighted in magenta, respectively. These edges form long-range order inside the particles, resulting in the skyrmionic vortex, [100] helices, and $[11\bar{1}]$ helices, respectively. In comparison between the observations (upper left panels of Fig. 4h–j) with their respective calculations (upper right panels), the observations do not contradict to the resultant projections of the simulations, corroborating the novel role of chiral geometric frustration in 0D.

Size and temperature dependence of skyrmionic vortex and helix

Although the particle size range in which the single skyrmionic vortex emerges is quite limited, the robustness of this state is dramatically improved as compared with that of the skyrmions in two- and one-dimensional geometries[19-21]. Figure 5a presents the observed in-plane magnetic fluxes in the $[01\bar{1}]$ projections in a matrix of temperatures and particle sizes. The magnetic states are robust against varying temperature with negligible configuration deviations. Some stripes typical for the helimagnetic state are invisible and supplanted by the skyrmionic closure textures below 200 nm in size. q-vectors of the observed helices are identified by comparison with the model-based imaging simulations for all of the q = <100>, <110>, and <111> propagations (Supplementary Fig. 5). The critical temperature of magnetic orderings somewhat decreased as the nanoparticle size is reduced, presumably because of the increasing contribution from the configurational instabilities near the surface.

Figure 5b summarizes these observations in the form of a magnetic phase diagram as functions of temperature and particle size, together with a phase diagram as a function of particle size deduced from the micromagnetic simulations. The simulated results reproduce the essential trend of the observed results, although some magnetic states are metastable because of the rather complicated energy landscape in small nanoparticles (for details, see the Supplementary note 2). The skyrmionic state is relatively stable as the particle size decreases and eventually becomes the ground state below 130 nm in size, as inferred from the micromagnetic simulation results. Within this size range, this state is robust from the magnetic ordering temperature (T_C) down to a cryogenic temperature

even in the absence of a magnetic field, indicating that the zero-dimensional chiral geometric frustration originating from the geometrical confinement plays a dominant role in stabilizing such topologically non-trivial magnetic configuration.

Summary and outlook

In summary, we investigated the intriguing and diverse magnetic structures geometrically confined in tetrahedral nanoparticles of skyrmion-hosting FeGe using EH imaging and micromagnetic simulations. This integrated approach, which combines observed and simulated imaging for multiple projection angles, revealed that the zero-dimensional confinement stabilizes an unconventional skyrmionic vortex state. The skyrmionic vortex exhibits a dramatically improved robustness throughout the temperature range below T_C without the application of any stimuli such as magnetic or electric fields. The results shed light on the unexplored role of zero-dimensional confinement on diverse magnetic and topological orders. This confinement offers a novel way to manipulate any desired number of skyrmionic vortices, thus providing a promising platform for skyrmionic engineering.

References and Notes:

1. Allwood, D. A. et al. Magnetic Domain-Wall Logic. *Science* **309**, 1688–1692 (2005).
2. Parkin, S. S. P., Hayashi, M. & Thomas, L. Magnetic Domain-Wall Racetrack Memory. *Science* **320**, 190–194 (2008).
3. Skyrme, T. H. R. A unified field theory of mesons and baryons. *Nucl. Phys.* **31**, 556–569 (1962).
4. Mühlbauer, S. et al. Skyrmion Lattice in a Chiral Magnet. *Science* **323**, 915–919 (2009).
5. Yu, X. Z. et al. Real-space observation of a two-dimensional skyrmion crystal. *Nature* **465**, 901–904 (2010).
6. Jonietz, F. et al. Emergent electrodynamics of skyrmions in a chiral magnet. *Nat. Phys.* **8**, 301–304 (2012).
7. Nagaosa, N. & Tokura, Y. Topological properties and dynamics of magnetic skyrmions. *Nat. Nanotechnol.* **8**, 899–911 (2013).
8. Fert, A., Cros, V. & Sampaio, J. Skyrmions on the track. *Nat. Nanotechnol.* **8**, 152–156 (2013).
9. Parkin, S. S. P. & Yang, S.-H. Memory on the racetrack. *Nat. Nanotechnol.* **10**, 195–198 (2015).
10. Liang, D., DeGrave, J. P., Stolt, M. J., Tokura, Y. & Jin, S. Current-driven dynamics of skyrmions stabilized in MnSi nanowires revealed by topological Hall effect. *Nat. Commun.* **6**, 8217 (2015).
11. Fert, A., Reyren, N. & Cros, V. Magnetic skyrmions: advances in physics and potential applications. *Nat. Rev. Mater.* **2**, 17031 (2017).
12. Sampaio, J., Cros, V., Rohart, S., Thiaville, A. & Fert, A. Nucleation, stability and current-induced motion of isolated magnetic skyrmions in nanostructures. *Nat. Nanotechnol.* **8**, 839–844 (2013).
13. Jiang, W. et al. Blowing magnetic skyrmion bubbles. *Science* **349**, 283–286 (2015).
14. Du, H. et al. Edge-mediated skyrmion chain and its collective dynamics in a confined geometry. *Nat. Commun.* **6**, 8504 (2015).
15. Jin, C. et al. Control of morphology and formation of highly geometrically confined magnetic skyrmions. *Nat. Commun.* **8**, 15569 (2017).

16. Zheng, F. et al. Direct Imaging of a Zero-Field Target Skyrmion and Its Polarity Switch in a Chiral Magnetic Nanodisk. *Phys. Rev. Lett.* **119**, 197205 (2017).
17. Iwasaki, J., Mochizuki, M. & Nagaosa, N. Current-induced skyrmion dynamics in constricted geometries. *Nat. Nanotechnol.* **8**, 742–747 (2013).
18. Zhao, X. et al. Direct imaging of magnetic field-driven transitions of skyrmion cluster states in FeGe nanodisks. *Proc. Natl. Acad. Sci.* **113**, 4918–4923 (2016).
19. Stolt, M. J. et al. Selective Chemical Vapor Deposition Growth of Cubic FeGe Nanowires That Support Stabilized Magnetic Skyrmions. *Nano Lett.* **17**, 508–514 (2017).
20. Yu, X. Z. et al. Near room-temperature formation of a skyrmion crystal in thin-films of the helimagnet FeGe. *Nat. Mater.* **10**, 106–109 (2011).
21. Mathur, N., Stolt, M. J. & Jin, S. Magnetic skyrmions in nanostructures of non-centrosymmetric materials. *APL Mater.* **7**, 120703 (2019).
22. Rybakov, F. N., Borisov, A. B. & Bogdanov, A. N. Three-dimensional skyrmion states in thin films of cubic helimagnets. *Phys. Rev. B* **87**, 094424 (2013).
23. Moon, K. et al. Spontaneous interlayer coherence in double-layer quantum Hall systems: Charged vortices and Kosterlitz-Thouless phase transitions. *Phys. Rev. B* **51**, 5138 (1995).
24. Tchernyshyov, O. & Chern, G.-W. Fractional Vortices and Composite Domain Walls in Flat Nanomagnets. *Phys. Rev. Lett.* **95**, 197204 (2005).
25. Bogdanov, A. N. & Rößler, U. K. Chiral Symmetry Breaking in Magnetic Thin Films and Multilayers. *Phys. Rev. Lett.* **87**, 037203 (2001).
26. Rohart, S. & Thiaville, A. Skyrmion confinement in ultrathin film nanostructures in the presence of Dzyaloshinskii-Moriya interaction. *Phys. Rev. B* **88**, 184422 (2013).

Methods:

Sample preparation. Nanostructures of FeGe structural polymorphs with a 1:1 Fe/Ge composition were synthesized using a chemical vapor deposition (CVD) method where the growth zone temperature of the reaction was set to 500–600 °C following a previously reported procedure[19]. Highly symmetric tetrahedral nanoparticles with various sizes (Fig. 1a, right column) were picked up on sharpened tungsten needles, and the needles were installed onto a lift-out grid (Fig. 2a). Particles greater than 300 nm in size were directly dispersed onto a lacey carbon grid and used for electron holography (EH) observations.

Electron holography. Electron holograms were formed by double-biprism interferometry[27] and recorded by a charge-coupled-device camera (UltraScan4000, GATAN) with a 300-kV transmission electron microscope (TEM) (HF-3300S, Hitachi). The EH observation angles and temperatures were coordinated using a double-tilt liquid-helium cooling holder (ULTDT, GATAN). The maximum of tilt angle β is ±18°. The mechanical configuration for the EH observation is illustrated in Supplementary Fig. 1a. As the opening angle without any mechanical interference was 50°±2° (Supplementary Fig. 1b), three systematic tilts through the $[010]$, $[01\bar{1}]$, and $[00\bar{1}]$ directions were feasible only by rotating α tilt, which is 360° rotatable and employed on the TEM goniometer, if the initial sample loading at $\alpha = 0°$ would satisfy nearly $[01\bar{1}]$ projection, as illustrated in Supplementary Fig. 1c. The exact tilt angles of the crystallographic orientations were preliminarily checked by nano-beam electron diffraction before cooling (Fig. 1l–n). We performed the liquid He transfer and consumed almost half of the filled liquid He for cooling the sample and capillaries at $\alpha = 0°$. The holder was then gradually tilted to $\alpha \sim \pm 45°$ to avoid exceeding the internal pressure resistance of the liquid He dewar. Our setup allows the lowest settled temperature of 10 K to be maintained for ~80 min with $\alpha \sim \pm 45°$. When the dewar was empty, it was refilled with liquid He after restoring the tilts.

For the hologram acquisition, the sample was slightly tilted away from the exact crystallographic (010), (011), and (001) planes to escape strong diffraction contrasts. During the heating sequence from 10 K, batches of multiple (> 20) holograms were recorded for the aimed projections at several settled temperatures of 10, 160, 240, 260,

and 293 K. Every batch of holograms was reconstructed into that of the phase images and averaged into one phase image after drift compensation. To subtract the phase shift due to the mean inner potential, the averaged phase images below the magnetic ordering temperature (T_C) (i.e., 10, 160, 240 and 260 K) were subtracted by the one at 293 K. A typical dataset of this protocol is provided in Supplementary Fig. 2. The fringe contrast and pitch were 18.9% and 5.5 nm, respectively. The resultant spatial and phase resolutions of the averaged reconstructed phase images were approximated to be 12.5 nm and 0.05 rad, respectively. In the phase reconstruction and subtraction processes, the correct magnetic phase shift was often not extracted from the fringe areas of nanoparticles and the supporting arm because of the abrupt change in traversing thickness, poor visibility, and/or slight deviation in the projection conditions at different temperatures. Such areas were masked with a transparent white color.

Model-based imaging simulations. Model-based imaging simulations were performed using the commercial ELF-MAGIC code. This code enabled the projection component (A_{pj}) of magnetic vector potentials $\boldsymbol{A}$ both inside and outside of the modeled magnetic building blocks to be calculated and integrated along the aimed projection direction. The A_{pj} distributions were calculated with respect to the [010], [01$\bar{1}$], and [00$\bar{1}$] projections.

The relation between the magnetic phase shift ($\Delta\varphi$) and the magnetic flux normal to the projection direction (i.e., in-plane: B_n) is given by

$$\Delta\varphi = \frac{e}{h/2\pi}\iint B_n dS$$

and from Stokes' theorem, we have

$$\oint \vec{A}\cdot d\vec{s} = \iint rot\vec{A}\cdot d\vec{S} = \iint B_n dS\,.$$

Therefore, we can derive the integrated in-plane magnetic flux B_n from the integrated A_{pj} and from $\Delta\varphi$[28]. The B_n distribution was displayed with color coding where the color hue and brightness represent the direction and density, respectively. For simplicity, the electrostatic potential of the blocks was set to be zero. The protocol is schematically presented in Supplementary Fig. 3.

Micromagnetic simulations. To investigate the magnetic ground state of B20-type FeGe tetrahedral nanoparticles, micromagnetic simulations were performed using the open-source software package MuMax3[29]. Material parameters were employed in the simulations with a saturation magnetization M_S = 384 kA/m, a spin-wave exchange stiffness constant A = 4.75 pJ/m, a Dzyaloshinskii–Moriya (DM) interaction strength D = 0.8527 mJ/m^2, a first-order cubic anisotropy K_c = −6 kJ/m^3, and a second-order cubic anisotropy K_{c2} = 12 kJ/m^3. The magnetic dipole−dipole interaction was taken into account to incorporate the effect of the tetrahedral shape. Nanoparticles ranging in size from 100 to 600 nm were constructed with 3 nm × 3 nm × 3 nm cubic cells. The surface anisotropy (uniaxial type with the axial direction normal to each surface) was also considered. Several ansatz were used for the initial spin textures: a random state, a single skyrmion state, a two-skyrmion state, a three-skyrmion state, a uniform state (with the spin direction along the z-axis), a helical state along the [001] direction, and a helical state along the [111] direction. After energy minimizations using the conjugate gradient method, the energies of different states were compared with each other to determine the ground state. To accurately reproduce the EH phase images, for the 145-nm tetrahedron, a surface anisotropy (easy-plane type) K_s = 95 μJ/m^2 and DM interaction with opposite chirality were included in the simulation. For the 185-nm tetrahedron, a reduced saturation magnetization M_S = 192 kA/m was employed. The simulated results were then inputted into the model-based imaging simulations and converted into the in-plane magnetic flux distributions along the [010], [01$\bar{1}$], and [00$\bar{1}$] directions to facilitate comparison with the experimental EH observations. For the protocol, see Supplementary Fig. 4.

Data availability:

The data that support the findings of this study are available within the article and its Supplementary Information. Any other relevant data are also available upon reasonable request from the corresponding authors.

References

27. Harada, K., Tonomura. A., Togawa. Y., Akashi. T. & Matsuda. T. Double-biprism electron interferometry. *Appl. Phys. Lett.* **84**, 3229 (2004).

28. Shindo. D. & Murakami. Y. Electron holography of magnetic materials. *J. Phys. D: Appl. Phys.* **41**, 183002 (2008).
29. Vansteenkiste. A. et al. The design and verification of MuMax3. *AIP Adv.* **4**, 107133 (2014).

Acknowledgments

K.N. was supported by Grant-in-Aids for Scientific Research (B) (No. 19H02418) and for Challenging Research (Exploratory) (No. 19K22052) from the JSPS. X.Z.Y. was supported by a Grant-in-Aid for Scientific Research (A) (No. 19H00660) from the JSPS and JST CREST (Grant Number: JPMJCR20T1). N.N. was supported by JST CREST (Grant Number: JPMJCR1874). A.C.B. and J.Z. acknowledge support from the U.S. Department of Energy (DOE), Office of Science, Basic Energy Sciences (BES) under Award No. DE-SC0020221. Y.L. was supported by the Special Postdoctoral Researcher program of RIKEN. N.M., M.J.S., and S.J. were supported by U.S. NSF grant ECCS-1609585. M.J.S. also acknowledges support from the NSF Graduate Research Fellowship Program.

Author contributions

S.J. and Y.T. conceived the project. N.M., M.J.S., and S.J. synthesised the FeGe nanoparticles. A.C.B., Y.L., and J.Z. performed the micromagnetic simulations. K.N. performed the EH observations and model-based simulations. K.N., Y.L., and J.Z. wrote the manuscript. All authors discussed the data and revised the manuscript.

Competing interests

The authors declare no competing interests.

Additional information

Supplementary information is available for this paper at http://***.

Correspondence and requests for materials should be addressed to K.N. or J.Z.

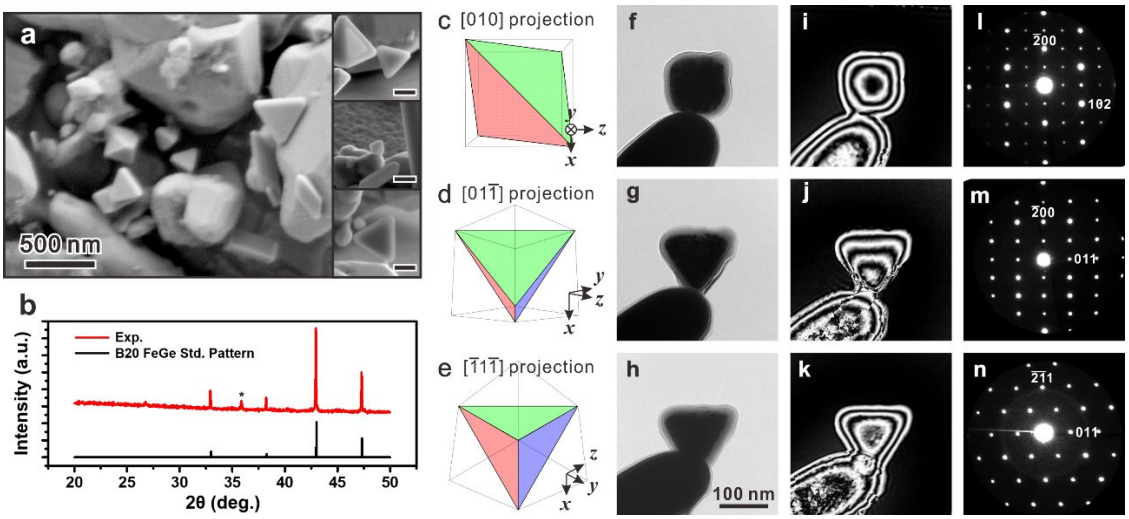

Fig. 1. Morphology and crystallography of FeGe tetrahedral nanoparticles synthesized by the CVD method. a, SEM images of the synthesized FeGe products. The right column presents magnified views of the well-faceted tetrahedral nanoparticles. (All scale bars in the insets are 200 nm.) **b**, XRD pattern obtained from the products and reference pattern for the B20 FeGe cubic crystal structure (JCPDS PDF no. 65-6357). The peak marked by the asterisk corresponds to the (120) peak of the hexagonal FeGe crystal structure of the faceted nanowires. **c–e**, Schematics of a tetrahedron projected along the [010], [01$\bar{1}$], and [$\bar{1}$1$\bar{1}$] directions. **f–h**, Corresponding TEM images. **i–k**, Corresponding phase (φ) maps taken at 293 K displayed in the form of cos(φ). **l–n**, Corresponding nanobeam diffraction patterns indexed with the [010], [01$\bar{1}$], and [$\bar{1}$1$\bar{1}$] zone axes.

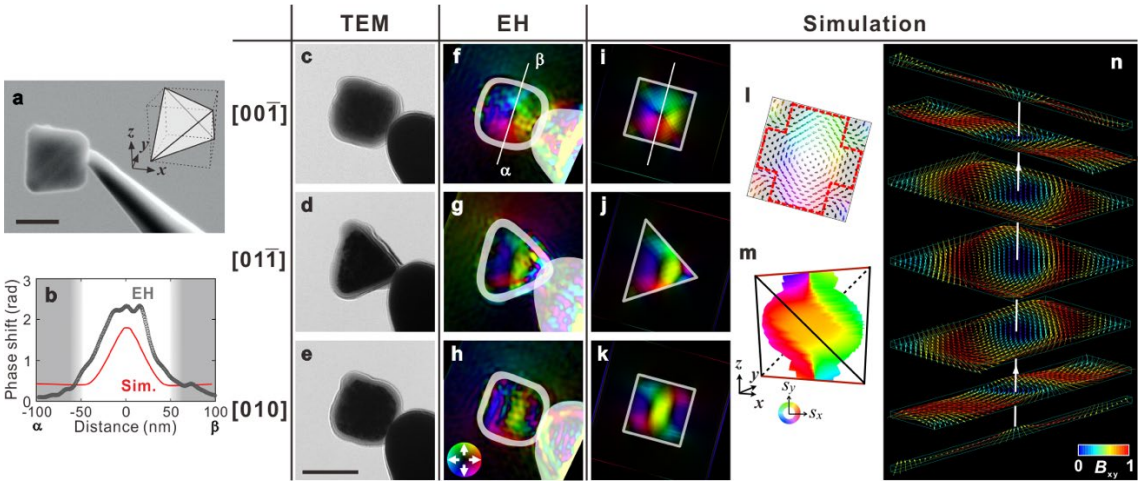

Fig. 2. Skyrmionic vortex confined in a 145-nm FeGe tetrahedral nanoparticle. a, A scanning electron micrograph showing a nanoparticle supported on a probe. The inset presents a schematic of the crystallographic orientation. **b**, Phase shift profiles along the lines in (**f**) and (**i**). **c**–**e**, TEM images along the $[00\bar{1}]$, $[01\bar{1}]$, and $[010]$ directions. **f**–**h**, Observed in-plane magnetic flux distributions for the corresponding projections at 10 K. Masked regions cover the fringes and probe, where phase reconstruction or subtraction fails because of the abrupt change in the traversing thickness, poor visibility, and/or slight deviation in the projection conditions at different temperatures. The color wheel in (**h**) represents the direction and magnitude of the projected in-plane magnetic flux. **i**–**k**, Corresponding projections of the micromagnetic simulations. **l**, Magnetic configuration of (**i**) integrated along the $[00\bar{1}]$ direction. **m**, Equi-spin surface with the *z*-component (*z* = [001]) of magnetization $S_z = 0$. **n**, Magnetic configurations in cross-sectional planes normal to the *z*-axis. All scale bars are 100 nm.

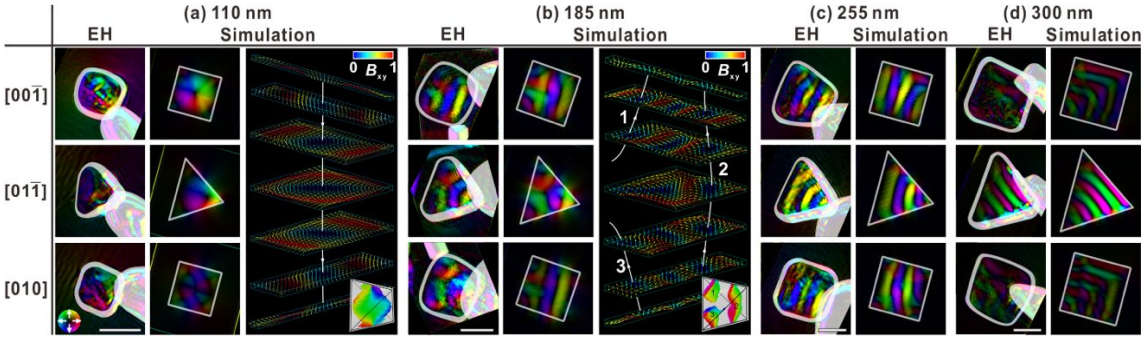

Fig. 3. Observations and simulations of non-trivial magnetic states projected along $[00\bar{1}]$, $[01\bar{1}]$, and $[010]$ directions. **a**, A 110-nm particle hosting a skyrmionic vortex. **b**, A 185-nm particle hosting three skyrmionic vortices. **c**, A 255-nm particle hosting $q = [100]$ helices. **d**, A 300-nm particle hosting $q = [111]$ helices. The scale bars are all 100 nm.

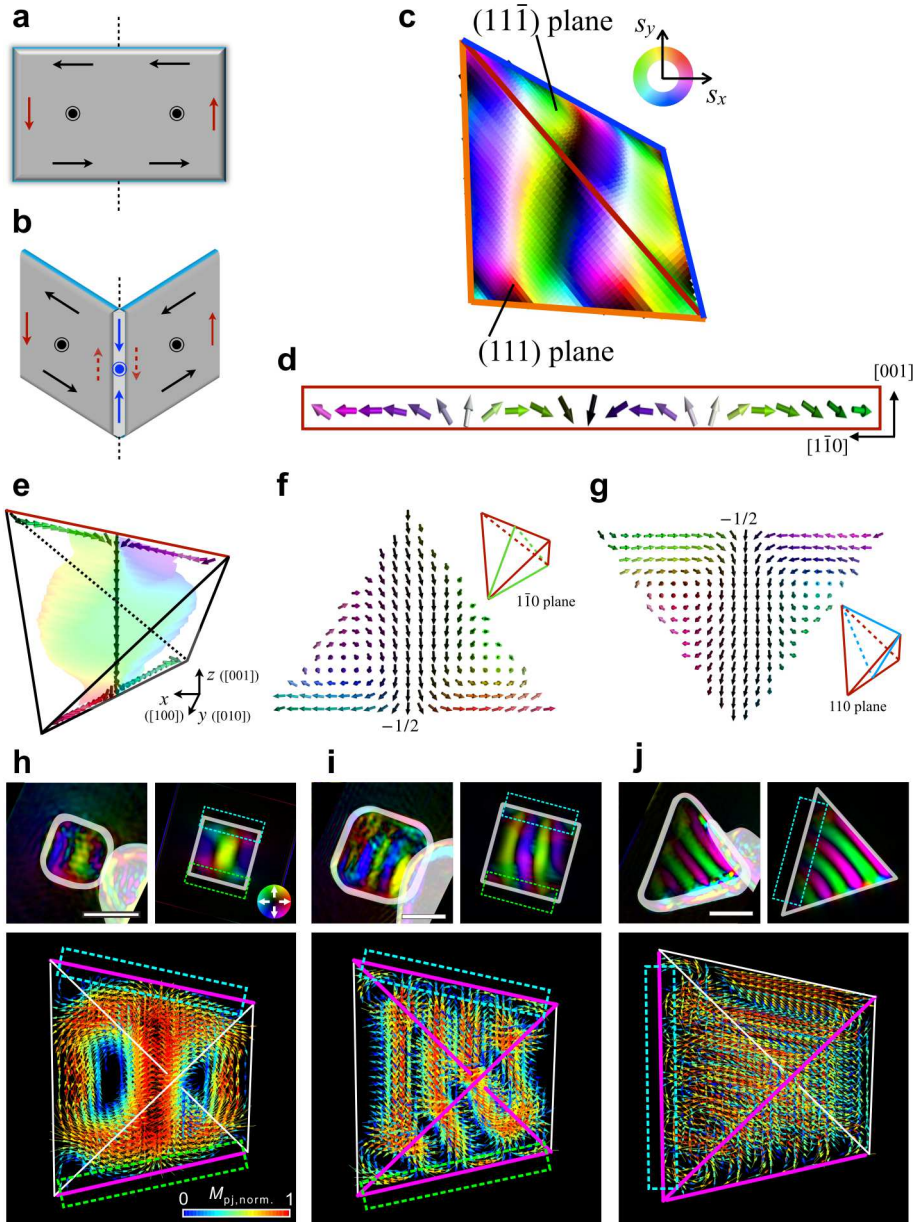

Fig. 4. Chiral edge state in tetrahedron. (**a** and **b**) Schematics of the spin twists at the edge in an (**a**) unfolded and (**b**) folded chiral magnet thin films. The black arrows and dots represent the helical stripe; the red arrows represent the directions of spin twist at the boundary; the blue ones represent a Néel-like edge spin twists formed as a consequence of chiral geometric frustration. **c**, Bird's-eye view of a helical $[100]$ state in a 210-nm tetrahedron. **d**, Edge spin twists on the top edge (red line in (**c**)) of tetrahedron. **e**, Edge spin twists with Néel-type domain walls at the top and bottom edges of a 145-nm tetrahedron. The formed skyrmionic vortex is shown as the light-colored tube. (**f** and **g**) Detailed spin distributions on the (**f**) $(1\bar{1}0)$ and (**g**) (110) planes. Fractional vortices with winding number $-\frac{1}{2}$ are emergent at the midpoints of horizontal edges. For clarity, the chirality and polarity

of the skyrmion shown here are opposite to those in Fig. 1. **h**, Néel-like edge spin twists forming a skyrmionic vortex in a 145-nm tetrahedron. **i**, Helices with $q = [100]$ in a 255-nm tetrahedron. **j**, Helices with $q = [11\bar{1}]$ in a 300-nm tetrahedron. In (**h**–**j**), upper left panels are the observed in-plane magnetic flux distributions projected along the $[010]$ direction; upper right panels are the counterparts obtained by micromagnetic simulations; lower panels are the simulated 3D magnetic configurations viewed along nearly the $[010]$ direction. The color of arrows refers to the color bar in the lower panel of (**h**) that represents the projected normalized magnetization $M_{pj,norm}$. Edges hosting the Néel-like spin twists are highlighted in magenta. Detailed magnetic configurations of the rectangles in the upper right panels of (**h**–**j**) are highlighted and shown in rectangles of the same color in the respective lower panels. The scale bars are all 100 nm.

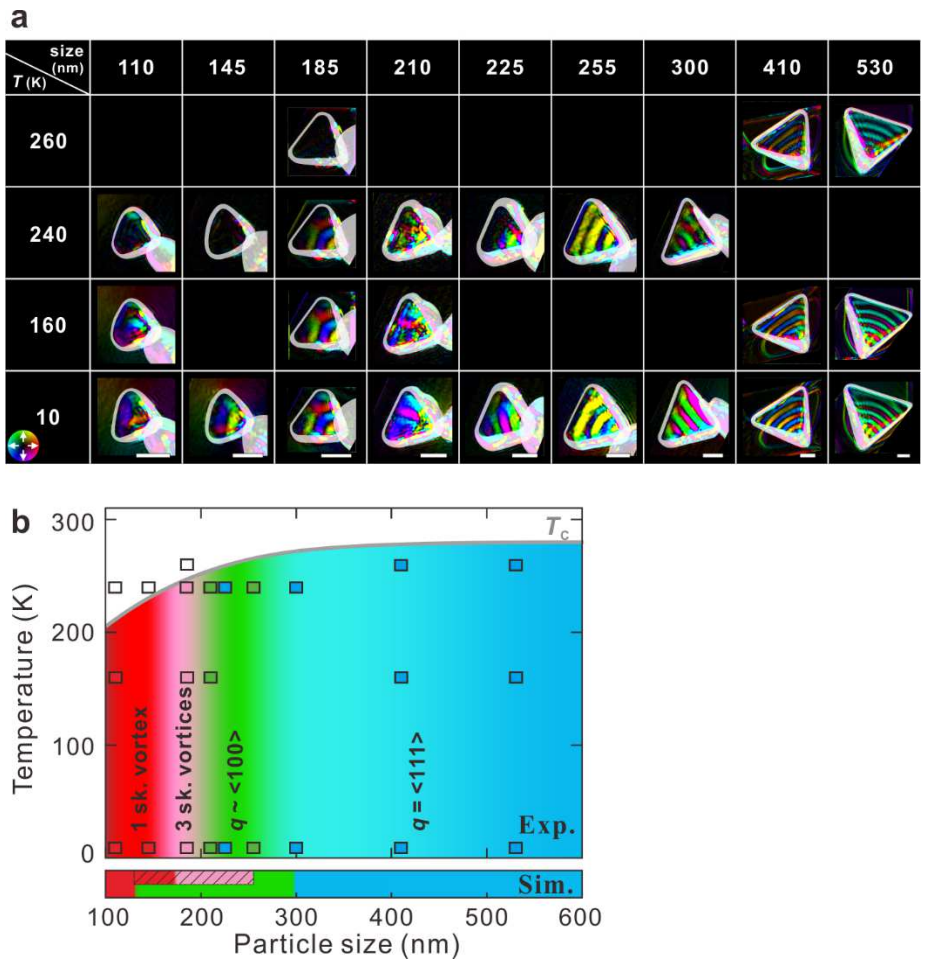

Fig. 5. Temperature and particle size dependence of magnetic textures. a, Observed in-plane magnetic fluxes along the $[01\bar{1}]$ direction in a matrix of temperatures and particle sizes. All scale bars are 100 nm. **b**, Magnetic phase diagram of FeGe tetrahedral nanoparticle system with respect to temperature and particle size. Each square represents an experimental observation data point. The bottom row represents the ground state deduced from micromagnetic simulations; the hatched region represents metastable states.

Figures

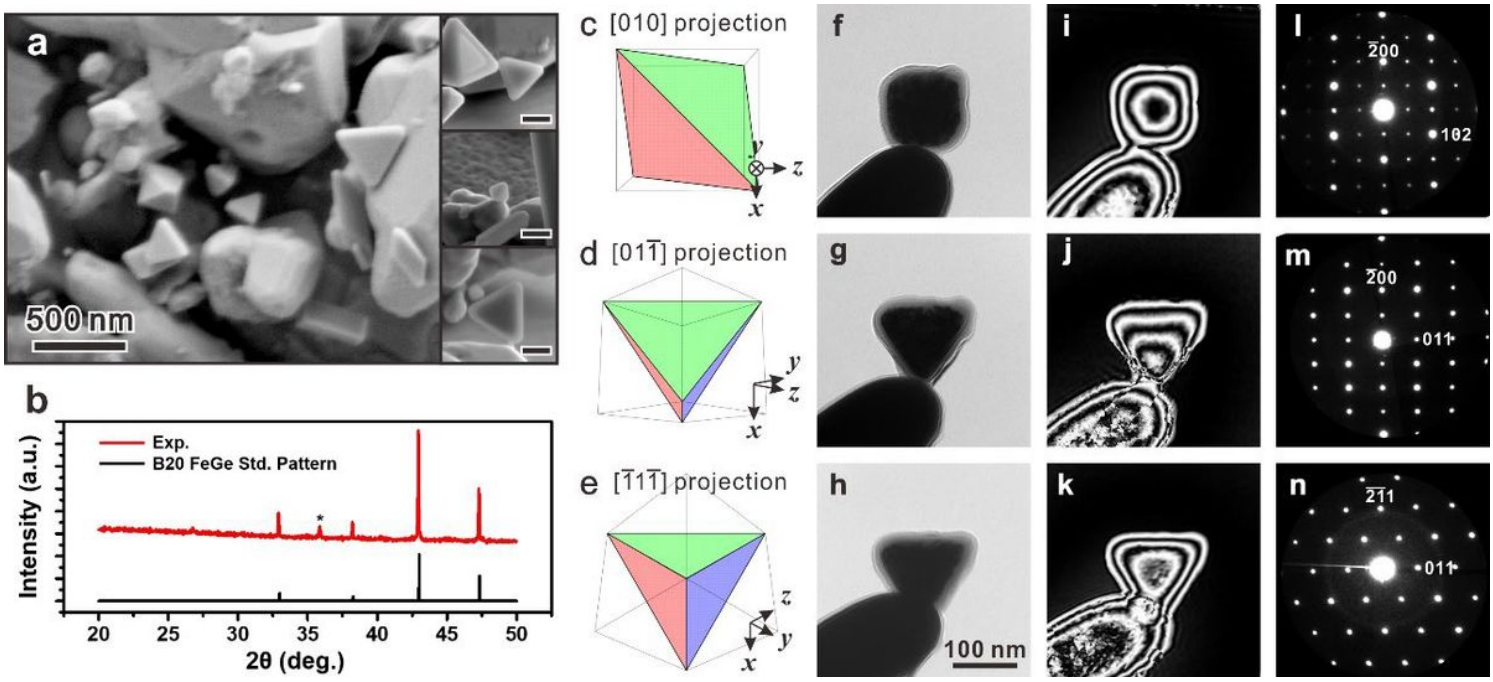

Figure 1

Morphology and crystallography of FeGe tetrahedral nanoparticles synthesized by the CVD method. (see Manuscript File for the full figure legend)

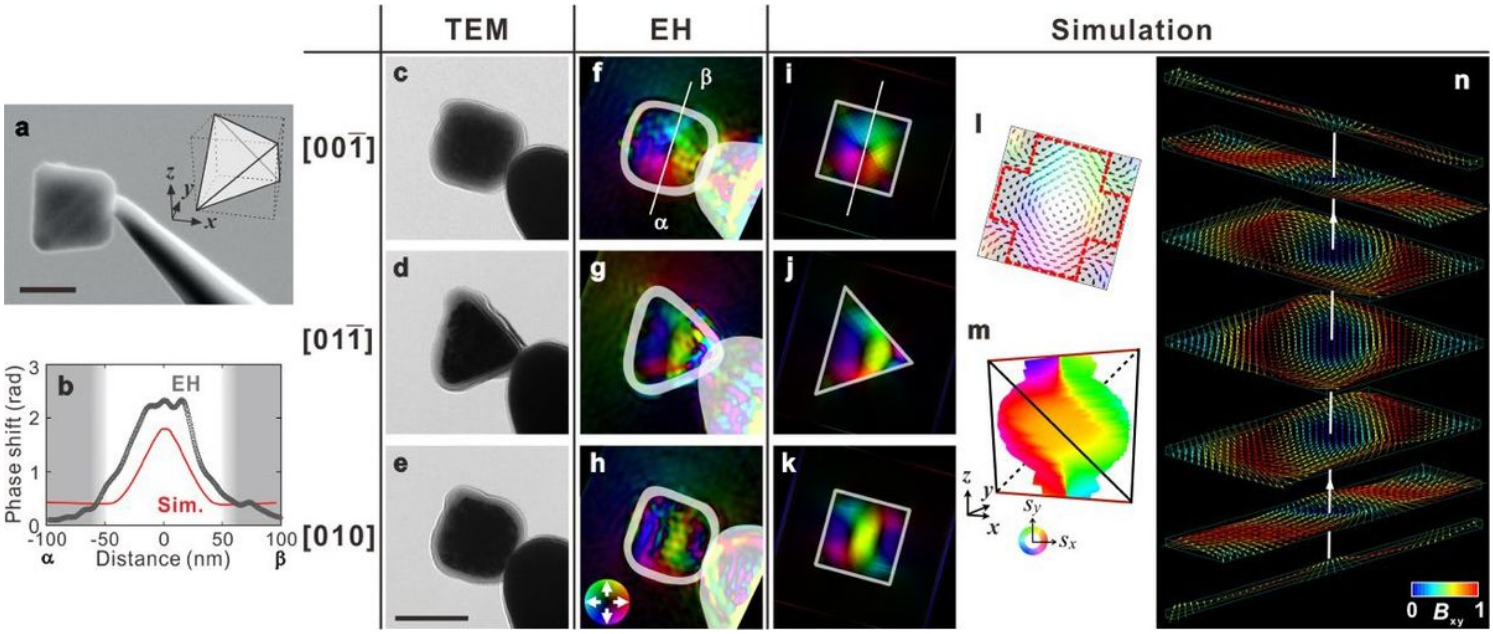

Figure 2

Skyrmionic vortex confined in a 145-nm FeGe tetrahedral nanoparticle. (see Manuscript File for the full figure legend)

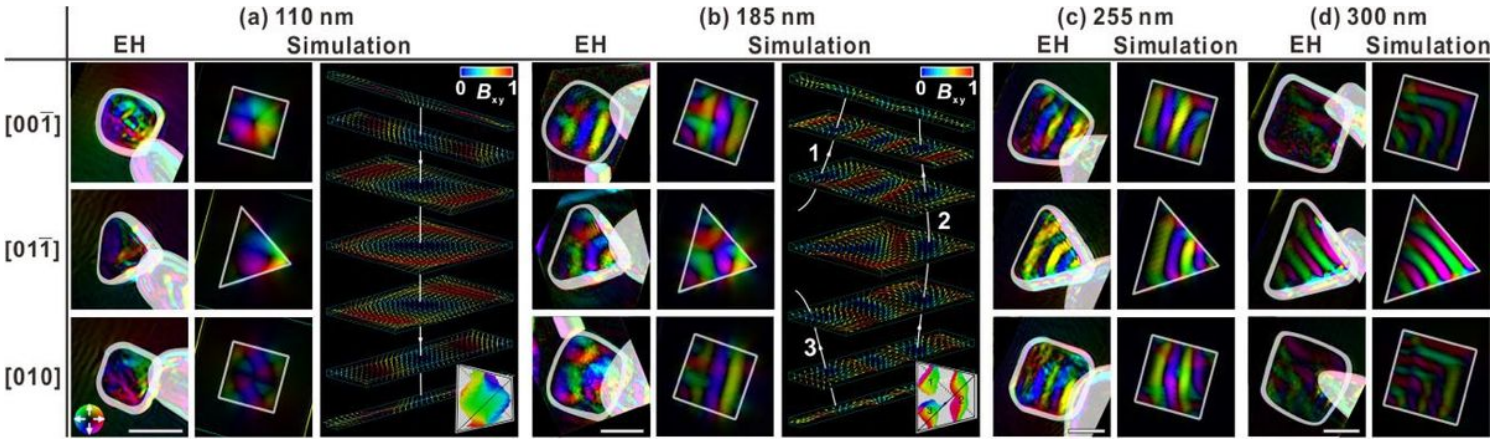

Figure 3

Observations and simulations of non-trivial magnetic states projected along [001], [011], and [010] directions. (see Manuscript File for the full figure legend)

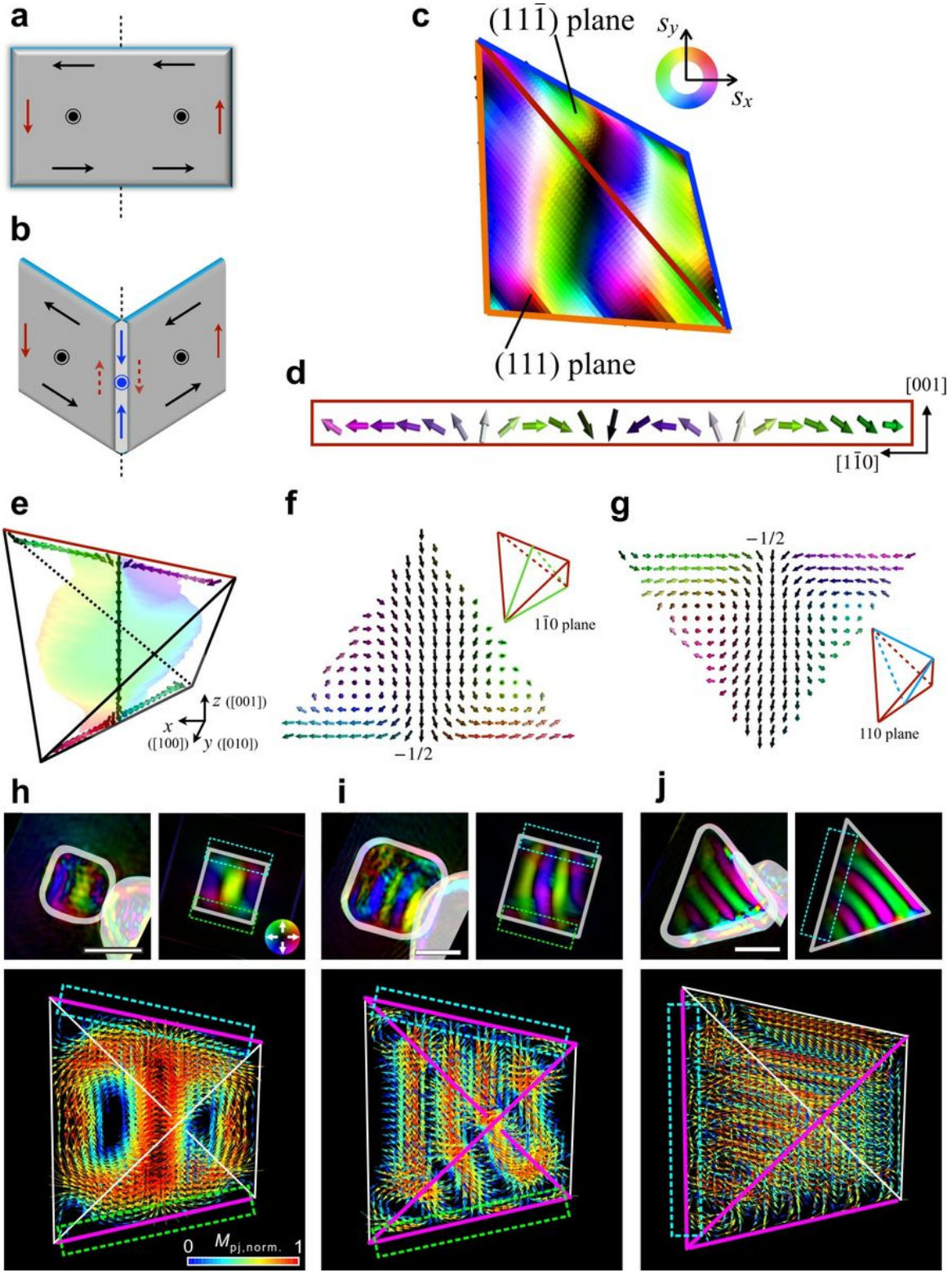

Figure 4

Chiral edge state in tetrahedron. (see Manuscript File for the full figure legend)

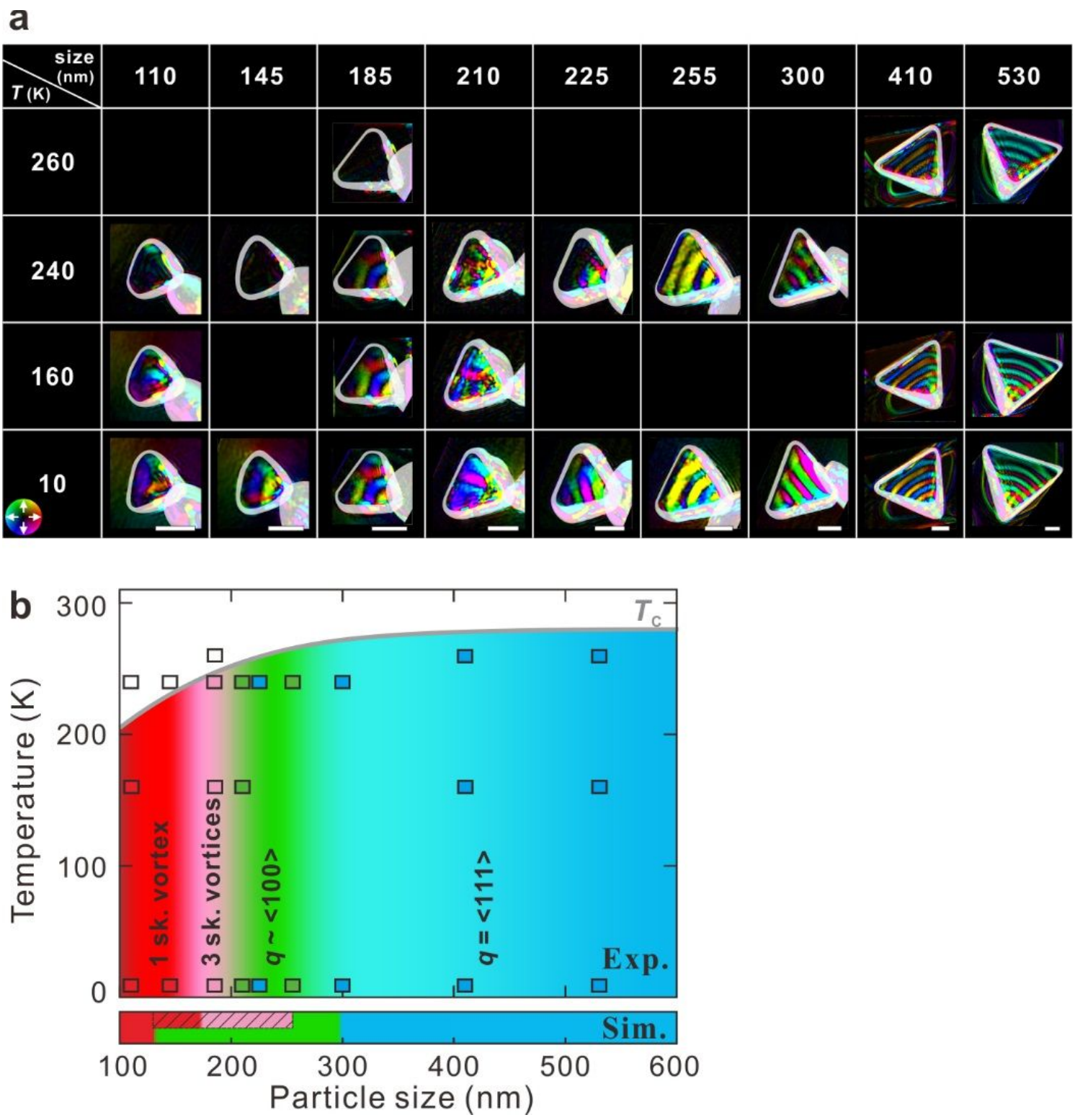

Figure 5

Temperature and particle size dependence of magnetic textures. (see Manuscript File for the full figure legend)

Supplementary Files

This is a list of supplementary files associated with this preprint. Click to download.

- Supplementary2.pdf
- 145tetraxyhigh.mov
- 145tetrazhigh.mov